1996ApJ...464..387H

THE ASTROPHYSICAL JOURNAL, 464:387–403, 1996 June 10
© 1996. The American Astronomical Society. All rights reserved. Printed in U.S.A.

SHEET MODELS OF PROTOSTELLAR COLLAPSE

LEE HARTMANN,[1] NURIA CALVET,[1,2,3] AND ALAN BOSS[4]
Received 1995 September 13; accepted 1995 December 27

ABSTRACT

Recognizing that protostellar clouds are unlikely to be completely spherical, we explore some effects of initial cloud geometry by considering collapse from a sheet initially in hydrostatic equilibrium. A qualitatively different feature of sheet collapse compared with spherical contraction is the development of relatively evacuated cavities in the infalling dusty cloud, which arise because material falls in first along the shortest dimension to the central gravitating mass. Using analytic models of collapse, which reproduce the main features of our previous numerical time-dependent simulations, we perform detailed radiative transfer calculations, which suggest that these collapse cavities can naturally explain the morphological appearance of many reflection nebulae around young stars on small distance scales without requiring initially diverging outflows. Sheet collapse models can simultaneously explain small-scale reflection nebula morphologies and dust envelope emission properties of many young stellar objects more easily than the standard spherical collapse models. The sheet collapse picture suggests that protostars, i.e., young stellar objects still accreting a large fraction of their mass from infalling envelopes, may be optically visible over a substantial range of system inclinations to the line of sight. These results may be especially relevant to cases where fragmentation and collapse has been triggered by an external impulse, such as a shock wave. We show how many properties of the flat-spectrum T Tauri star HL Tau can be interpreted in terms of flattened protostellar cloud collapse and draw some distinctions between the flattened toroids resulting in our calculations and the "pseudodisk" of Galli & Shu.

Subject headings: circumstellar matter — stars: formation — stars: pre–main-sequence

1. INTRODUCTION

Theoretical calculations of protostar formation generally start from an initially spherical cloud for simplicity (e.g., Larson 1972; Appenzeller & Tscharnuter 1974; Shu 1977; Bodenheimer & Black 1978; Boss 1980; Terebey, Shu, & Cassen 1984, hereafter TSC, and references therein). However, observations suggest that star-forming molecular cloud cores are usually elongated (Myers et al. 1991), as might be expected if an initial sheetlike or filamentary geometry plays an essential role in the required fragmentation of molecular clouds into single and multiple stellar systems (Larson 1985; Bonnell & Bastien 1992; Boss 1993). Because any initial departure from spherical symmetry is likely to be magnified during gravitational collapse, investigations of the role of the initial cloud geometry in protostar formation are needed.

In a recent paper (Hartmann et al. 1994, hereafter Paper I) we presented an initial exploration of protostellar collapse from a flattened cloud. We considered the time-dependent axisymmetric evolution of a marginally Jeans-unstable region in an isothermal, nonmagnetic, nonrotating, self-gravitating sheet (Fig. 1). Starting from a configuration in hydrostatic equilibrium (Fig. 1, *upper left*), the sheet contracted subsonically to form a central mass concentration (Fig. 1, *upper right*). Once an appreciable gravitating mass was formed at the center (the protostar), the remaining cloud material began to collapse at nearly free-fall velocities, and the infalling envelope became increasingly flattened and toroidal in appearance (Fig. 1, *bottom panels*).

An important aspect of collapse from a sheet, which differs qualitatively from contraction of an initially spherical distribution of material, is the appearance of two "bipolar" cavities on either side of the central plane of the sheet (Fig. 1, *bottom panels*). The cavities result simply because the regions closest to the central mass fall in before material from distant regions in the plane of the sheet can reach the center. Similar infall cavities were found in the simulations of the collapse of a rotating, magnetized filamentary cloud by Nakamura, Hanawa, & Nakano (1995).

These cavities are particularly interesting because a large body of evidence points to the existence of "holes" or paths of very low extinction though dusty protostellar envelopes. For example, the morphologies of reflection nebulae around many young stellar objects often suggest conical or bowl-shaped cavities carved into dense, dusty material that cannot plausibly be produced by rotation (Whitney & Hartmann 1993). Although powerful bipolar outflows must escape through envelopes (Staude & Elsässer 1993; Whitney & Hartmann 1993; Kenyon et al. 1993b, hereafter KWGH), the observed jets are highly collimated (e.g., Masson & Chernin 1993), and it is not clear how they can produce the wide opening angles of many reflection nebulae. Sheet collapse may produce the required envelope cavities naturally without *any* outflow.

The cavity structure resulting from sheet collapse implies that the extinction to the central source, expected to be large during protostellar collapse (e.g., Larson 1972; Appenzeller & Tschnarnuter 1974; Adams, Lada, & Shu 1987), may depend strongly on system inclination. The standard TSC model for the collapse of a rotating, initially spherical protostellar envelope, predicts only a modest dependence of the envelope extinction of the central protos-

[1] Harvard-Smithsonian Center for Astrophysics, 60 Garden Street, Cambridge, MA 02138; hartmann@cfa.harvard.edu.
[2] Five College Astronomy Department, Amherst, MA; calvet@decoy.phast.umass.edu.
[3] On leave from Centro de Investigaciones de Astronomia, Mérida, Venezuela.
[4] DTM, Carnegie Institution of Washington, 5241 Broad Branch Road, NW, Washington, DC 20015-1305; boss@dtm.ciw.edu.

© American Astronomical Society • Provided by the NASA Astrophysics Data System

1996ApJ...464..387H

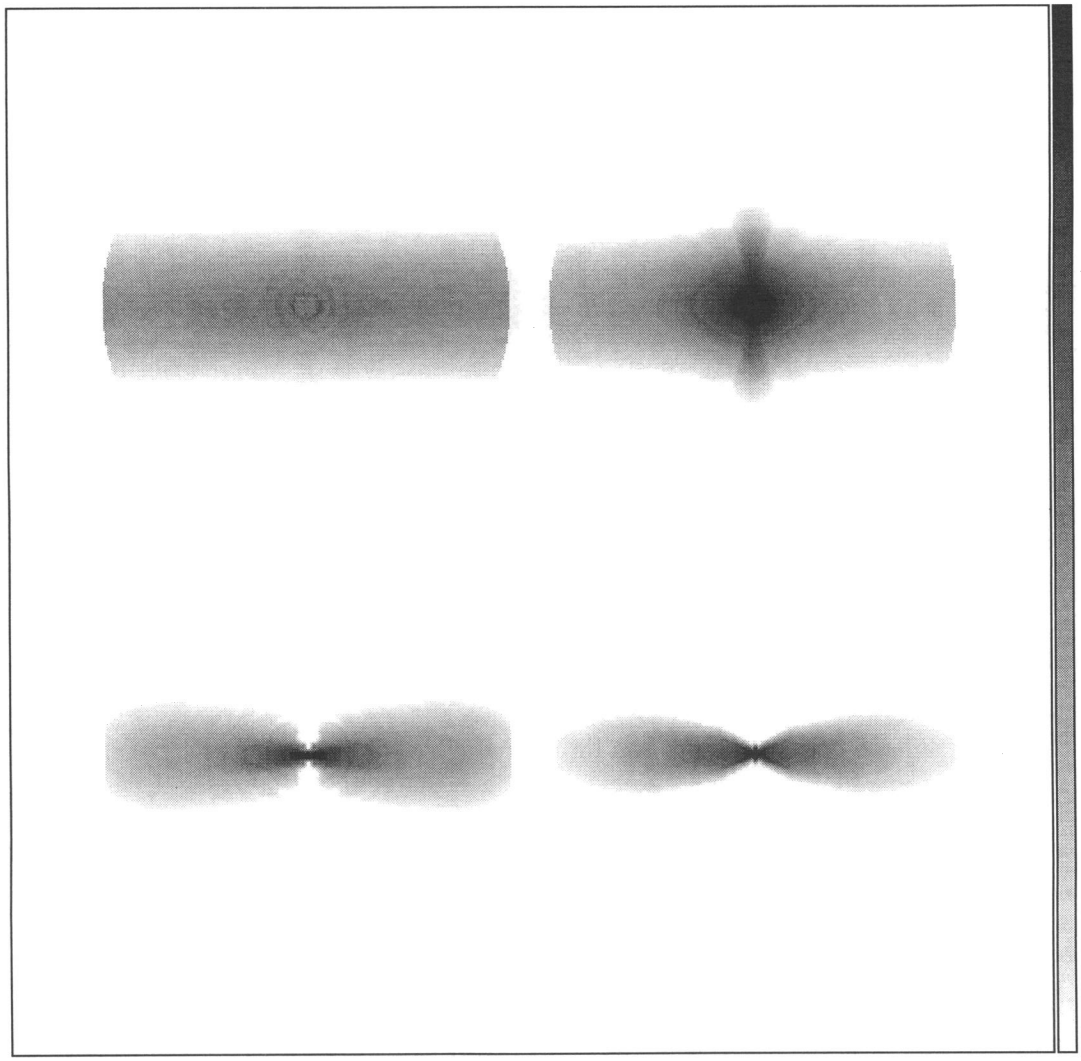

FIG. 1.—Gray-scale representation of the density distribution of the numerical simulation in Paper I, measured in a meridional plane. The initial density distribution is that of an isothermal self-gravitating, infinite layer; the simulation is bounded by a spherical surface that does not allow material from the outside to fall in. The radius of this surface is just large enough that the enclosed material is gravitationally unstable (see text). In the upper left, after 2.7 free-fall times ($=1.2 \times 10^5$ yr), the layer still retains its basic hydrostatic equilibrium configuration as material begins to fall in. After 6 free-fall times, a dense central concentration of modest flattening builds up (*upper right*). By 6.5 free-fall times (*lower left*), the material along the central axis has collapsed, producing an evacuated region perpendicular to the plane of the layer. The density distribution continues to flatten at 7 free-fall times (*lower right*), resulting in a toroidal density distribution.

tar on inclination—roughly a factor of 2. In contrast, the central source extinction in the sheet collapse model can vary by an order of magnitude or more as a function of inclination to the line of sight.

The inclination dependence of extinction in flattened collapse models suggests that protostars—i.e., objects that have yet to accrete much of their final masses from infalling envelopes—could actually be optically visible over a fairly wide range of viewing angles. We have previously suggested that the optically visible flat spectrum T Tauri stars (such as HL Tau and T Tau itself) are protostars, and that the far-infrared excess emission of these objects is due to thermal radiation from dust in infalling envelopes (Calvet et al. 1994). This suggestion is supported by interferometric observations of HL Tau, which seem to indicate infalling material in a highly flattened geometry (Hayashi, Ohashi, & Miyama 1993). Conversely, protostars viewed near the equatorial plane of the original sheet might appear especially highly extincted; such a model might help explain the most heavily extincted young stellar objects, the so-called "Class 0" objects (Andre, Ward-Thompson, & Barsony 1993).

There are other potentially significant observational implications of nonspherical collapse. For example, elongated, large-scale infalling envelopes could be common if fragmentation from sheets or filaments is essential to the star-formation process; and such structures, in the absence of definitive kinematic information, might be misinterpreted as "disks" even though they are not rotationally supported. In the context of magnetically resisted collapse from a spherical cloud, Galli & Shu (1993a, 1993b) first pointed out the possibility of infalling flattened structures on large scales. Sheet collapse models naturally produce toroids or geometrically thick infalling "disks." These sheet toroids differ from the Galli & Shu (1993a, 1993b) "pseudodisks," as the latter structures are geometrically thin; therefore, sheet toroids and pseudodisks will have different observational signatures.

In this paper we explore some of the observational consequences of the sheet collapse model presented in Paper I. To

© American Astronomical Society • Provided by the NASA Astrophysics Data System

1996ApJ...464..387H

this end we develop an approximate analytic model that modifies the basic results of Paper I to include rotation. We compute the scattered light and thermal emission from these dusty envelope models, assuming the energy source heating the envelope is at the center. We show that sheet collapse models can simultaneously match scattered light images and spectral energy distributions of individual objects much more easily than TSC models modified by bipolar outflow holes. In § 2 we present our sheet infall model, in § 3 we present radiative transfer results for typical protostars, in § 4 we develop specific models for individual objects to show the power of the flattened collapse hypothesis in detail, and in § 5 we briefly consider more general implications of nonspherical collapse.

2. FLATTENED COLLAPSE MODEL

2.1. *Basic Model*

We wish to treat the collapse of a nonspherical protostellar cloud in a simple way that conveniently allows us to explore some observational consequences with a minimum of computation. Although a wide variety of initial conditions can be imagined (see Boss 1993, and references therein), for simplicity we follow Paper I in considering axisymmetric collapse from an isothermal, nonmagnetic, infinite self-gravitating sheet in hydrostatic equilibrium. The numerical methods used were described by Boss & Myhill (1992). We neglect magnetic fields, not because they are necessarily dynamically unimportant, but to provide the nonspherical analog of the TSC nonmagnetic infall solutions. TSC models have provided the basis for numerous studies of protostellar spectral energy distributions (e.g., Adams & Shu 1986; Adams, Lada, & Shu 1987, 1988; Butner et al. 1991; Butner, Natta, & Evans 1994; Kenyon, Calvet, & Hartmann 1993a, hereafter KCH; KWGH; Calvet et al. 1994), suggesting that nonmagnetic collapse models can be fruitfully employed in initial explorations. (We consider the possible application of these models to the more general case of magnetized collapse in § 5.) Radiation pressure is negligible for the cool central objects and low protostellar luminosities considered here (see, e.g., Wolfire & Cassinelli 1987).

We consider only axisymmetric collapse to make the radiative transfer calculations tractable. Nonaxisymmetry in the outer envelope should be negligible for a cloud that collapses to form a single star—that is supported by detailed three-dimensional hydrodynamic models (see Figs. 3 and 5 in Boss 1993). Although real clouds are unlikely to be precisely axisymmetric, for our purposes we require only that a region with radial size $r \sim (3\text{–}4)H$ be axisymmetric, where H is the scale height of the original sheet. This is because we consider only early phases of protostellar infall, such that more distant regions have not fallen in to the center (all of the emission we calculate for comparison with observations originates within $r \lesssim H$).

In the numerical simulation in Paper I we restricted the calculation to a volume just larger than the Jeans length and did not allow material external to this volume to enter. However, the gravity of the external (infinite) sheet was included to ensure that the structure was stable for a few free-fall times. Since the sheet is isothermal, and the Jeans length scales with the density scale height of the matter, one can regard this simulation as providing results that can be scaled to different values of the gas temperature; all such simulations would have similar geometrical aspect ratios at times scaled with the free-fall time (or the sound crossing time).

Under these assumptions, the mass infall rates scale as c_s^3, where c_s is the isothermal sound speed, just as in the case of spherical cloud collapse (Shu 1977). We have verified this result by direct numerical calculation; the basic physics can be understood from a simple argument due to J. Tsai (1995, personal communication). The density distribution of the isothermal sheet in hydrostatic equilibrium is

$$\rho(z) = \rho(0)\ \mathrm{sech}^2\ (z/H)\ , \tag{1}$$

where $\rho(0)$ is the midplane mass density and z is the distance from the midplane, and the scale height H is defined by

$$H = c_s^2/(\pi G\Sigma)\ , \tag{2}$$

where Σ is the total surface density (Spitzer 1978, p. 283). The mass of the cloud is given by

$$M_c = \pi\Sigma R_{\rm out}^2 = \pi\Sigma(\eta_{\rm max} H)^2\ , \tag{3}$$

where $\eta_{\rm max} = R_{\rm out}/H$, and $R_{\rm out}$ is the limiting radius of our computational volume (no flow-through at the outer boundary). Combining these equations we have

$$M_c = \frac{\eta_{\rm max}^2 c_s^4}{\pi G^2 \Sigma}\ . \tag{4}$$

Then, assuming the collapse time is comparable to the sound crossing time, as it must be on dimensional grounds for a medium thermally supported against gravity,

$$\dot{M} \sim \frac{M_c}{\eta_{\rm max} H/c_s} = \eta_{\rm max}\frac{c_s^3}{G}\ . \tag{5}$$

The cloud will be gravitationally unstable to axisymmetric perturbations if $\eta_{\rm max} > 3.83$ (Larson 1985). Because we assumed initial conditions close to a stable hydrostatic equilibrium in our numerical simulation, we adopted an initial value of $\eta_{\rm max} \approx 4$, just larger than this limiting value. In our numerical simulation the mass infall rate is never exactly constant, but there is a "plateau" phase where the infall rate does not vary much from about $\dot{M} \sim 6 \times 10^{-6}$ $M_\odot\ {\rm yr}^{-1}$. Inserting numbers for a pure molecular hydrogen gas at 10 K, we find that the mass infall rate predicted by equation (5) is $\sim 8 \times 10^{-6}\ M_\odot\ {\rm yr}^{-1}$, comparable to the plateau phase infall rate in the numerical simulation.

This result may be compared with the constant mass infall rate for the isothermal singular sphere of $\dot{M} = 0.975 c_s^3/G$ found by Shu (1977). The scaling of the infall rate depends similarly on the sound speed in the case of sheet collapse, but the constant of proportionality differs because of the difference in geometry. The singular isothermal sphere at $T = 10$ K exhibits a constant infall rate of $\dot{M} \sim 2 \times 10^{-6}\ M_\odot\ {\rm yr}^{-1}$, while our non–self-similar collapse has a time-varying infall rate, decreasing with increasing elapsed time (see Paper I).

We may scale the numerical results to other situations provided the basic initial conditions remain similar—that is, the cloud is part of an isothermal self-gravitating sheet, initially in hydrostatic equilibrium, with a mass just larger than the Jeans mass. Because the critical maximum radial wavenumber for instability is a fixed ratio of the scale height H, it follows that all similar solutions will have the same

© American Astronomical Society • Provided by the NASA Astrophysics Data System

1996ApJ...464..387H

ratio of outer radius R_{out} to H, i.e., they will have the same η_{max}. Using the numerical results as a calibration, we estimate

$$\dot{M} \approx 6 \times 10^{-6}(T/10\ \mathrm{K})^{3/2}\ M_\odot\ \mathrm{yr}^{-1} \quad (6)$$

and

$$M_c \approx (T/10\ \mathrm{K})^2(\Sigma/9 \times 10^{-2}\ \mathrm{g\ cm}^{-2})^{-1}\ M_\odot\ . \quad (7)$$

For reference, we note that in our standard 10 K case, $H \sim$ 1600 AU and the outer radius of the original axisymmetric cloud was $\sim 4H$.

2.2. *Rotating Collapse*

To calculate the predicted emission from sheet collapse models in a reasonably accurate way, we need to extend the results of Paper I to finer spatial grids near the central protostar than generally feasible with hydrodynamic calculations for the entire envelope (see Yorke, Bodenheimer, & Laughlin 1993 for a discussion). We also need to modify the results of Paper I to include rotation, because the angular momentum of the collapsing cloud plays a crucial role in determining the extinction through the inner envelope (see discussion in Adams et al. 1987). Our strategy is to assume that rotation plays a small role at large scales, as also assumed in the TSC solutions, so that we can use the results of Paper I to calibrate our large-scale density structure, while modifying the solution on small scales to account for the angular momentum barrier. Here we develop an analytic model that accounts for rotation and can also be divided into a sufficiently fine spatial grid for the calculation of the inner envelope emission.

The results of the numerical calculations in Paper I suggest that after collapse has proceeded for some time, free-fall from an initially flattened layer toward a central point mass provides a useful approximation to the more detailed hydrodynamic calculations. Although the flat layer collapse and the TSC model differ considerably on large scales, the behavior of the inner regions of both the TSC model and the sheet collapse model in later stages can be understood in terms of free-fall toward a central mass. We are therefore motivated to explore an approximate model for the inner regions of flat layer collapse, in which the main features of the rotating TSC solution are retained, but the flattening of the outer envelope produces an additional angular dependence of the density distribution.

The inner regions of the TSC protostellar collapse model are described by the solution of Cassen & Moosman (1981, hereafter CM) and Ulrich (1976), hereafter jointly referred to as CMU. In the CMU solution the gas in falls freely toward a central point mass, following essentially parabolic paths that terminate at the rotational equator (the disk). The streamlines in the meridional plane are labeled by $\mu_0 = \cos\theta_0$, where θ_0 is the angle between the rotational axis and the streamline at large radial distances. It is convenient to determine the solution by specifying velocities and densities at a (distant) reference radius r_0. The velocity at this reference radius is nearly equal to the radial free-fall value, with a small azimuthal component corresponding to constant angular velocity at r_0. The density is constant at r_0 (spherically symmetric), and set by the required mass infall rate $\dot{M}$. With these assumptions, the density of the inner envelope at $(r, \mu = \cos\theta)$, where r is the radial distance from the central mass and θ is the position angle measured from the rotational symmetry axis of the system, is given by

$$\rho_{CMU}(r, \mu) = \frac{\dot{M}}{4\pi(GMr^3)^{1/2}}\left(1 + \frac{\mu}{\mu_0}\right)^{-1/2}\left(\frac{\mu}{\mu_0} + \frac{2\mu_0^2}{r/R_c}\right)^{-1}\ . \quad (8)$$

Here $\dot{M}$ is the mass infall rate and R_c is the so-called "centrifugal radius." The equation of the streamlines relates μ, μ_0, and r/R_c:

$$\frac{r}{R_c} = \frac{(1 - \mu_0^2)}{1 - \mu/\mu_0}\ . \quad (9)$$

At large distances $r \gg R_c$, $\mu \to \mu_0$, the motions are radial, and equation (8) reduces to the usual spherical density distribution for radial free-fall from rest at constant mass infall rate. For $r \lesssim R_c$, the motions become significantly nonradial, and the angular momentum of the infalling material causes it to land on a disk ($\mu = 0$) at radial distances between $0 \le r \le R_c$. The density distribution follows directly by assuming mass conservation in steady flow along flow tubes bounded by streamlines $\mu_0 =$ constant, which are radial at large distances but curve appreciably near R_c (see CM).

We now suppose that the initial cloud is not spherically symmetric at r_0. We take the initial density distribution to be proportional to that of our nonrotating, isothermal, self-gravitating layer in hydrostatic equilibrium, which should be a reasonable approximation if the initial angular velocity is small. To make things especially simple we assume that the rotation axis is perpendicular to the plane of the self-gravitating layer, so that the density distribution of the infalling material will be axisymmetric. Then, the initial sheet density at the reference radius can be written as

$$\rho_S(r_0(t), \mu_0) = \rho_0\ \mathrm{sech}^2\ (r_0\,\mu_0/H)\ . \quad (10)$$

If we take the infall rate from the numerical simulation, we can write the density of the infalling envelope in terms of ρ_{CMU}, the CMU density distribution for a the same $\dot{M}$ and R_c:

$$\rho_S(r, \mu) = \rho_{CMU}(r, \mu)\ \mathrm{sech}^2\ (\eta\mu_0)[\eta/\tanh\ (\eta)]\ , \quad (11)$$

where the terms in the final bracket represent the normalizing constant needed to produce the same $\dot{M}$ in each model. As shown in Figure 2, this simple modification introduces an smooth angular modulation of the CMU density

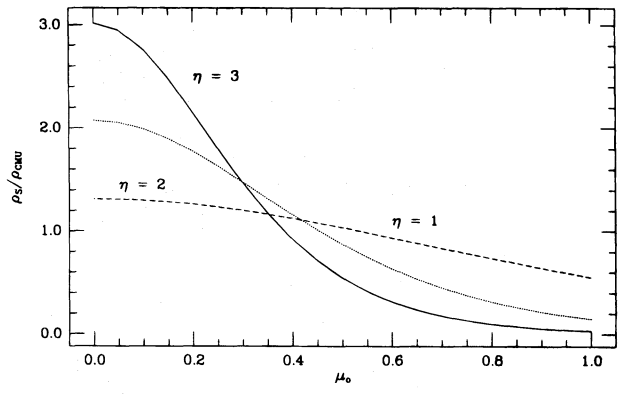

FIG. 2.—Angle-dependent modification of the CM density distribution adopted for the radiative transfer models, parameterized by the value of η (see text).

© American Astronomical Society • Provided by the NASA Astrophysics Data System

1996ApJ...464..387H

distribution, with lower densities along the axis of symmetry (equal to the rotation axis).

Figure 3 shows the angle-averaged density for the CMU and η cases, adjusted to have the same $\dot{M}$. The effect of a larger η is to evacuate the infalling envelope inside of R_c; material originating near the plane of symmetry falls preferentially near R_c, while polar material, which is reduced substantially from the CMU case at large η, falls in to the disk plane at $r < R_c$ (see streamlines in CM).

How well does this simple modification of the CMU infall model reproduce the numerical results on large scales? To make a comparison we require input values of $\dot{M}$ and the central point mass. In the simulation the central mass is growing with time; for purposes of comparison we have adopted 0.5 of the instantaneous central mass as the appropriate average mass for the sheet collapse model. Since the density for a given infall rate varies only as the inverse of the square root of the central mass, which is not varying rapidly during the portion of envelope evolution being considered, the choice of average mass is not crucial. For this comparison with the nonrotating numerical results, we have adopted a sufficiently small centrifugal radius ($R_c = 5.8$ AU) that the effects of rotation are negligible on the size scales displayed.

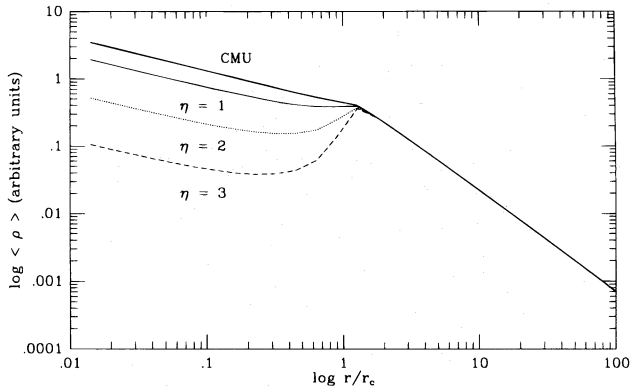

FIG. 3.—Angle-averaged density distribution in arbitrary units for the CMU and η models. Inside the centrifugal radius R_c the angular momentum of the infalling material causes departures from simple radial free fall $\rho \propto r^{-3/2}$. Larger values of η reduce the density distribution inside of R_c more than in the outer regions (see text).

Figure 4 shows comparisons between the simulation in Paper I at two points in time with sheet collapse models. The overall properties of the density distribution are approximately reproduced with the appropriate choice of the parameter η. The agreement is reasonable, especially when one considers that this solution is really only valid for regions much smaller than the outer cloud radius. The model works better at later times than at earlier times, partly because there are substantial departures from radial free-fall motions during the initial stages of collapse. The most notable difference between the model and the numerical simulation is that the simulation shows more evacuation along the axis of symmetry. In the numerical calculations, pressure forces initially cause the inflowing material to travel parallel to the plane of symmetry, not radially toward the center. Eventually, this material collides at the symmetry axis of the system (see Fig. 1, *upper right*) and plunges rapidly to the center, leaving behind an evacuated region along the axis. The simple radial pressureless collapse model cannot reproduce this complicated, time-dependent behavior of the simulation. At later times, when the central

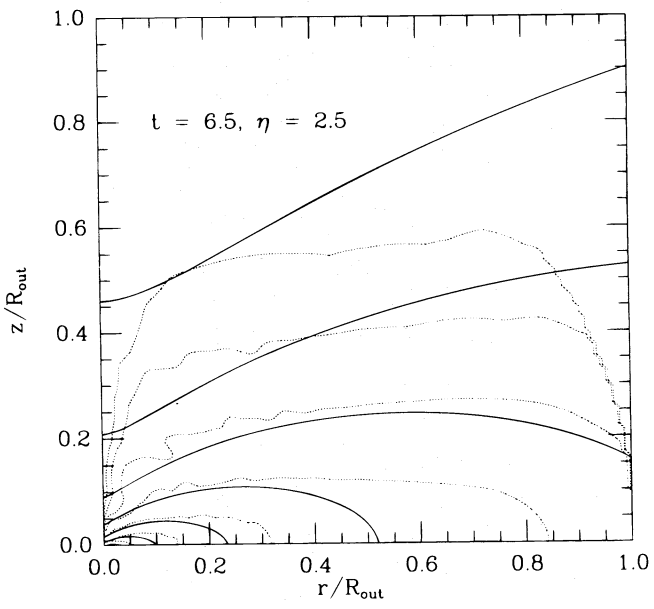

FIG. 4a

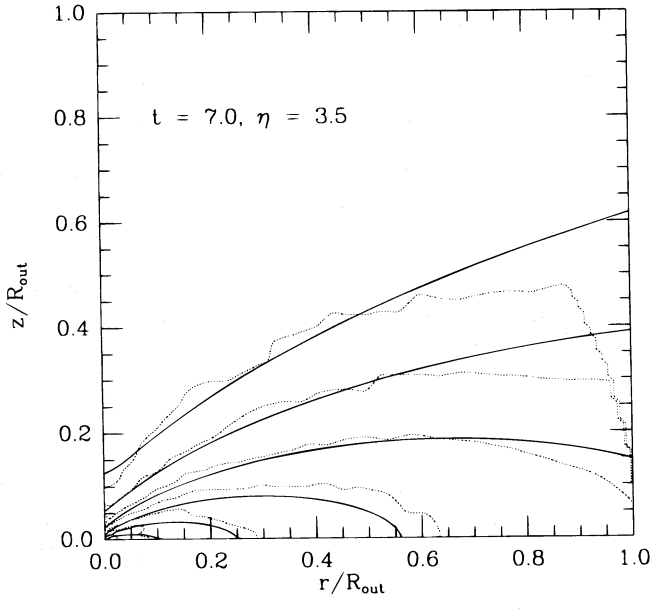

FIG. 4b

FIG. 4.—Comparison between the density distributions of the numerical simulation and sheet models. The spatial dimensions are given in units of the outer radius of the cloud $R_{out} = 8.6 \times 10^{16}$ cm. In (*a*), the numerical density distribution at a time of 6.5 free-fall times $= 3 \times 10^5$ yr is compared with the density distribution of a sheet model characterized by a mass infall rate $6 \times 10^{-6}\ M_\odot\ \mathrm{yr}^{-1}$, a central mass of 0.21 $M_\odot$ (half that of the central mass in the numerical simulation), and $\eta = 2.5$. The lowest density contour corresponds to a molecular hydrogen number density of $10^4\ \mathrm{cm}^{-3}$, and subsequent contours represent factors of $10^{1/2}$ increase in density. Panel (*b*) shows a similar comparison between the numerical results at $t = 7t_{ff} = 3.2 \times 10^5$ yr and a sheet collapse model with the same infall rate, a central mass of 0.32 $M_\odot$ (again half the mass of the central cell in the numerical calculations), and $\eta = 3.5$. The sheet model reproduces the overall behavior of the numerical simulation reasonably well, except that the numerical results show a more highly evacuated region near the symmetry axis because of time-dependent pressure forces (see text).

© American Astronomical Society • Provided by the NASA Astrophysics Data System

1996ApJ...464..387H

mass has grown, and therefore gravitational forces more strongly dominate pressure forces, the simple pressureless model works better (Fig. 4*b*).

Our modified-CMU prescription cannot precisely treat the detailed time evolution of the infalling envelope while the central mass is changing substantially. Qualitatively, η must increase with time, because as the collapse proceeds material from larger initial radii r_0 arrives at the central regions. The case of sheet collapse is more complicated than the inside-out collapse of TSC because there is no well-defined "beginning" time of collapse; the absence of an initial central concentration in density, coupled with the departures from spherical symmetry, preclude a simple expansion-wave solution as in TSC.

As discussed in the previous subsection, cloud collapse, once initiated, occurs on a sound crossing time, and this in turn suggests that $r_0 \sim c_s \Delta t$, so that $\eta = r_0/H$ should increase roughly linearly with the time Δt elapsed after the initial core formation. The numerical calculations scale approximately this way. The two simulations shown in Figure 4 can be matched with $\eta \sim 2.5$ and $\eta \sim 3.5$ models, which would imply that r_0 has moved outward by about H. Moving at the sound speed, this evolution should take about 3.4×10^4 yr, while the two snapshots shown in Figure 4 are separated by an elapsed time of about 2.6×10^4 yr, or about $\frac{3}{4}$ of this time. Given the approximate nature of our calculation, which neglects the change in central mass as a function of time, nonradial motions, and any gravitational attraction from the rest of the envelope, this level of agreement is reasonable.

The maximum amount of flattening of the envelope during evolution depends upon the adopted geometry. Within the context of collapse from a self-gravitating infinite isothermal sheet in hydrostatic equilibrium, the minimum wavelength for instability scales with the scale height H, regardless of the surface density or temperature (see Larson 1985). Restricting our exploration to sheet models that are just barely gravitationally unstable demands that $\eta \leq \eta_{\max} \sim 4$ (see previous section), independent of the cloud mass. The numerical simulations for later stages of the infall suggest a match with $\eta \sim 3$–4, which is consistent with the expected $\eta \sim \eta_{\max}$. (We have a non–flow-through outer boundary condition, so that material exterior to $R_{\rm out}$ cannot fall in to the central star. If we had chosen a larger outer radius, the collapse would evolve to even flatter configurations; however, in this case the initial cloud would have had a mass much larger than a Jeans mass and would have been strongly unstable from the outset of the calculation.)

To summarize, the simple parameterized sheet collapse model provides a reasonable first approximation to the numerical infall solutions for flat, self-gravitating layers initially in hydrostatic equilibrium and just barely gravitationally unstable. (We have not directly tested the effects of rotation on the solution, but the CMU theory should be applicable to the flattened cloud case.) The detailed evolution of η and $\dot{M}$ with time can be scaled from the numerical solutions for similar initial conditions; in general, one expects the mass infall rate to scale as c_s^3, and the flatness parameter η to increase roughly linearly with time until it is $\sim \eta_{\max}$. This approximation provides a simple and fast way to vary the (small) angular momentum of the cloud to explore the combined effects of (small) rotation and geometry on observable quantities.

3. RADIATIVE TRANSFER RESULTS FOR TYPICAL PROTOSTELLAR SOURCES

Next, we use the infall model developed in the previous section as a basis for radiative transfer calculations to illustrate the basic effects of flattened geometry on the dust emission from protostellar envelopes. The envelope dust emission depends directly on the density, not the mass infall rate, so we use a parameter ρ_1, which is the density the infalling material would have at 1 AU if there were no rotation; thus, $\rho_1 \propto \dot{M}/M^{1/2}$ (see eq. [8]). We adopt a value $\rho_1 = 3 \times 10^{-14}$ g cm^{-3}, which is the median value found for the protostellar (Class I) sources in the Taurus-Auriga molecular cloud (KCH, KWGH). The implied infall rate toward a central mass of 0.5 $M_\odot$ is 4×10^{-6} $M_\odot$ yr^{-1}, comparable to the quasi-steady rate $\sim 6 \times 10^{-6}$ $M_\odot$ yr^{-1} found in the numerical simulation of the sheet collapse of Paper I. We further adopt a centrifugal radius $R_c = 50$ AU, which is comparable to the median value of $R_c \sim 70$ AU estimated for Taurus Class I sources using TSC models (KCH, KWGH).

The emission at $\lambda \lesssim 1$ μm is dominated by light produced by the central source and scattered out of the infalling envelope. We computed the scattered light images using Monte Carlo methods described in Whitney & Hartmann (1992, 1993), which take into account nonisotropic scattering phase functions and calculate both intensity and polarization. In the present paper we restrict our results to the J band ($\lambda = 1.25$ μm), using the "MRN" dust parameters discussed in Whitney & Hartmann (1992) and KCH.

Thermal dust emission was calculated using our previously discussed methods (KCH; Calvet et al. 1994). Our "1.5-dimensional" solutions use a spherically averaged radiative equilibrium temperature distribution, but incorporate the exact density distribution of the dusty envelope to calculate emergent fluxes. Initial results for two-dimensional, axisymmetric radiative equilibrium temperature calculations indicate relatively modest differences from the 1.5-dimensional approach for model parameters of interest here (see also Efstathiou & Rowan-Robinson 1991 and Chick, Pollack, & Cassen 1996).

3.1. *Scattered Light Images*

Figure 5 shows J band (1.25 μm) images and polarization patterns for sheet models with the above parameters and $\eta = 1, 2, 3, 4$, viewed at an inclination of $i = 60°$ to the line of sight. The images have been convolved with a Gaussian point spread function with a full width at half-maximum of 1 pixel (28 AU) to smooth the results slightly.

These images show that the sheet collapse models naturally produce reflection nebulae that appear to have large opening angles. As discussed in § 3.2, values of $\eta \sim 2.5$–3.5 are characteristic of the envelope density distribution during the main infall phase, which would produce very open cavities. Since η should increase with increasing time, the sequence shown in Figure 5 corresponds to a time sequence, suggesting that the opening angle of reflection nebulae should increase with increasing age. The polarization patterns are generally centrosymmetric, with some departures near the highest extinction regions from multiple scattering (Whitney & Hartmann 1993).

Figure 5*b* displays images for $\eta = 3$ and two different viewing angles. When observed more pole-on, a central point source is evident, with a faint reflection nebula sur-

© American Astronomical Society • Provided by the NASA Astrophysics Data System

1996ApJ...464..387H

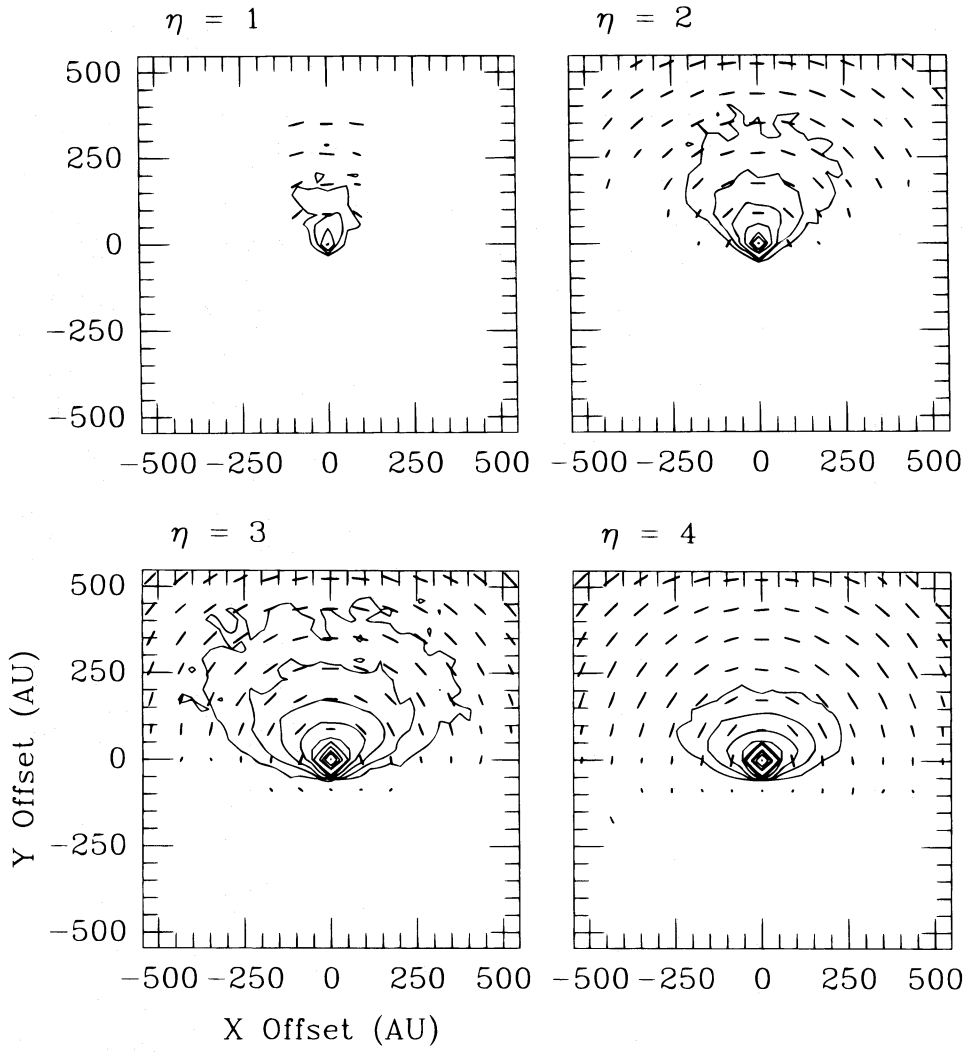

FIG. 5a

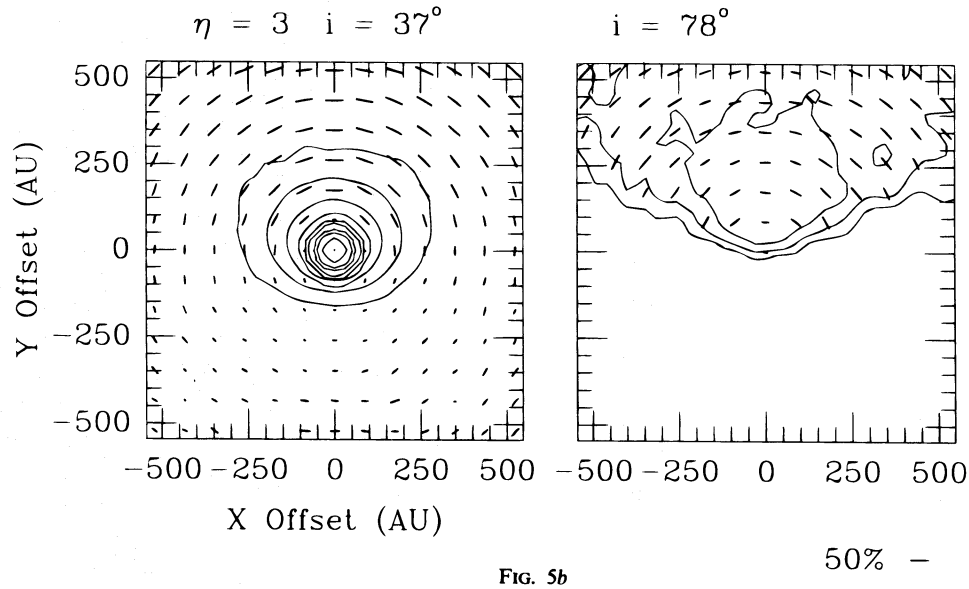

FIG. 5b

FIG. 5.—(*a*) Images and polarization maps at 1.25 μm, $i = 60°$, for the $\eta = 1, 2, 3, 4$ models with $\dot{M} = 4 \times 10^{-6}\ M_\odot\ \mathrm{yr}^{-1}$, $R_c = 50$ AU, and $M = 0.5\ M_\odot$, assuming MRN dust parameters (see text). The opening angle of the reflection nebula increases with increasing η. Global scattering results for these models at various inclinations are given in Table 1. (*b*) Same as (*a*), except at $i = 37°$ and $i = 78°$

© American Astronomical Society • Provided by the NASA Astrophysics Data System

1996ApJ...464..387H

rounding it. At large inclination angles, the central point source is completely obscured, and all that is visible is a diffuse reflection nebula. The back side cavity cannot be observed, given the number of photons run through the model, because the envelope is so strongly extincting.

Table 1 summarizes the scattering model properties at a variety of viewing angles. At high inclinations (edge-on), the polarizations tend to be large because relatively small amounts of direct unpolarized light from the central star escape from the envelope. At low inclinations (pole-on), the contribution of direct light from the central star dominates and the polarization is low. When the envelopes are not very flattened, the polarization is perpendicular to the axis of symmetry (negative values); for more flattened envelopes (larger η), the plane of polarization can change to become parallel to the axis of symmetry (positive values of P) (Fig. 5).

TABLE 1

SCATTERING RESULTS

η	cos i	I	P	Error
1.....	0.0	1.96E−04	−0.31	±0.04
1.....	0.1	2.35E−04	−0.32	±0.02
1.....	0.2	2.60E−04	−0.27	±0.02
1.....	0.3	3.36E−04	−0.28	±0.02
1.....	0.4	4.70E−04	−0.22	±0.02
1.....	0.5	6.95E−04	−0.17	±0.01
1.....	0.6	1.18E−03	−0.12	±0.01
1.....	0.7	2.09E−03	−0.072	±0.005
1.....	0.8	3.98E−03	−0.041	±0.002
1.....	0.9	7.81E−03	−0.017	±0.002
1.....	1.0	1.18E−02	−0.005	±0.002
2.....	0.0	7.14E−04	−0.30	±0.02
2.....	0.1	8.45E−04	−0.31	±0.02
2.....	0.2	1.31E−03	−0.27	±0.007
2.....	0.3	2.48E−03	−0.24	±0.006
2.....	0.4	4.79E−03	−0.19	±0.003
2.....	0.5	1.13E−02	−0.11	±0.002
2.....	0.6	3.03E−02	−0.052	±0.001
2.....	0.7	7.22E−02	−0.023	±0.0003
2.....	0.8	0.143	−0.010	±0.0002
2.....	0.9	0.240	−0.0028	±0.0002
2.....	1.0	0.325	−0.0009	±0.0001
3.....	0.0	4.78E−04	−0.19	±0.02
3.....	0.1	7.64E−04	-0.19	±0.01
3.....	0.2	2.01E−03	−0.15	±0.002
3.....	0.3	5.26E−03	−0.11	±0.002
3.....	0.4	1.99E−02	−0.041	±0.002
3.....	0.5	8.01E−02	−0.0081	±0.002
3.....	0.6	0.214	0.0012	±0.0002
3.....	0.7	0.393	0.0041	±0.0002
3.....	0.8	0.576	0.0035	±0.0002
3.....	0.9	0.734	0.0019	±0.0002
3.....	1.0	0.844	0.0003	±0.0002
4.....	0.0	2.10E−04	−0.089	±0.009
4.....	0.1	5.59E−04	−0.073	±0.037
4.....	0.2	2.33E−03	−0.032	±0.003
4.....	0.3	0.011	0.0074	±0.001
4.....	0.4	0.080	0.016	±0.0007
4.....	0.5	0.271	0.014	±0.0001
4.....	0.6	0.505	0.012	±0.0001
4.....	0.7	0.695	0.0091	±0.0001
4.....	0.8	0.837	0.0065	±0.0001
4.....	0.9	0.944	0.0036	±0.0001
4.....	1.0	1.02	0.0010	±0.0001

NOTE.—The observed intensity I is the ratio of the total observed flux to that which would be received if the star were unobscured; it can be larger than unity at low inclinations for large η models because of extra scattering by the envelope into the line of sight. The polarization P is negative when perpendicular to the symmetry (y) axis and is positive when parallel to the symmetry axis. All fluxes and polarizations are measured in an aperture of radius 1400 AU.

The basic properties of these scattered light images are similar to those found by Whitney & Hartmann (1993) for scattering from a TSC infall envelope with a cavity. The polar cavities employed by Whitney & Hartmann were completely evacuated; the edge of the cavity was given by the streamlines for a given $\theta_0 = \theta_w$, where θ_w was the opening half-angle of the wind at large distances. In effect, the present models are also streamline hole models, except that the polar cavities are not completely evacuated and do not exhibit a sharp edge in density. Given this approximate correspondence, it is not surprising that many of the properties of the models are similar.

When the envelope is very flattened ($\eta = 4$), the polarization becomes quite small and the central star is relatively unextincted at a wide variety of inclination angles. The scattered-light image of this model is quite flat, and suggests something like a "flared disk" (Kenyon & Hartmann 1987; Lazareff, Pudritz, & Monin 1990). But this structure is not a rotationally supported disk; it arises naturally from the assumed initial conditions of gravitational collapse from an initially sheetlike cloud geometry.

3.2. *Spectral Energy Distributions*

Figure 6*a* shows the spectral energy distributions (SEDs) of models with $R_c = 50$ AU, and $\eta = 2$ (*upper panel*) and $\eta = 3$ (*lower panel*) at different inclinations. All models shown have $\rho_1 = 3 \times 10^{-14}$ g cm^{-3}, a total luminosity of 5 $L_\odot$, and an envelope radius of 10^4 AU. The system luminosity arises entirely from the central star. For comparison, we also show in Figure 6*a* TSC models with the same values of ρ_1, R_c and envelope radius. The main effect of the flattened geometry is to increase the escape of optical and near-infrared radiation at low inclinations relative to the spherical collapse, due to the larger evacuation of the polar regions. At very high inclinations, in contrast, the sheet models produce lower near- and mid-infrared fluxes than the TSC model with the same ρ_1, reflecting the higher concentration of material toward the equatorial plane (see Fig. 2). At submillimeter wavelengths and longer, the emission comes from the large-scale, optically thin regions, which are essentially similar in the TSC and the sheet models, so fluxes are the same.

The increase of polar evacuation and the corresponding lower values of the optical depth at low inclinations make the near-infrared fluxes higher for the larger η models. For inclinations $\lesssim 30°$, the silicate feature appears in emission in the $\eta = 3$ model and the SED becomes "double peaked" with a minimum in the continuum around 10 μm, an appearance that has been interpreted as indicative of the presence of gaps in disks (Mathieu, Adams, & Latham 1991). This question will be investigated further in a subsequent paper.

Figure 6*b* shows SEDs for similar envelope models as Figure 6*a*, but with the addition of a standard steady accretion disk, with an accretion luminosity $\frac{1}{2}$ of the total luminosity of the system. Emission from the disk increases the system flux in the near-infrared; this extra emission is more conspicuous at lower inclinations and the higher η (more flattened) cases (compare with Fig. 6*a*).

Initially spherical collapse (TSC) models require values of R_c between ~ 70 AU and 300 AU to explain the observed SEDs of Taurus sources (KCH; Calvet et al. 1994). The

© American Astronomical Society • Provided by the NASA Astrophysics Data System

1996ApJ...464..387H

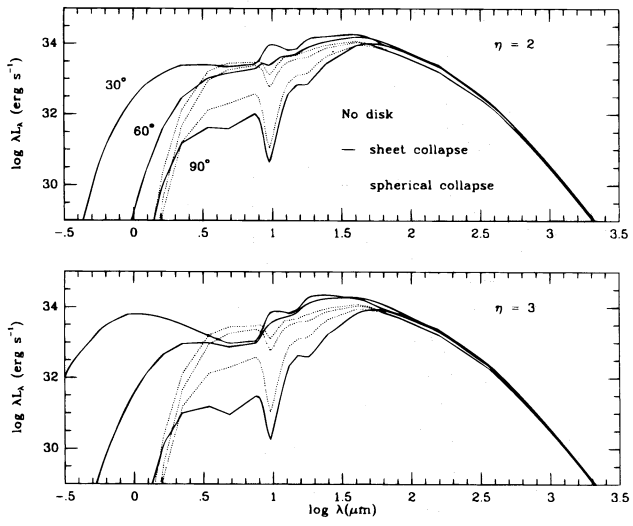

FIG. 6a

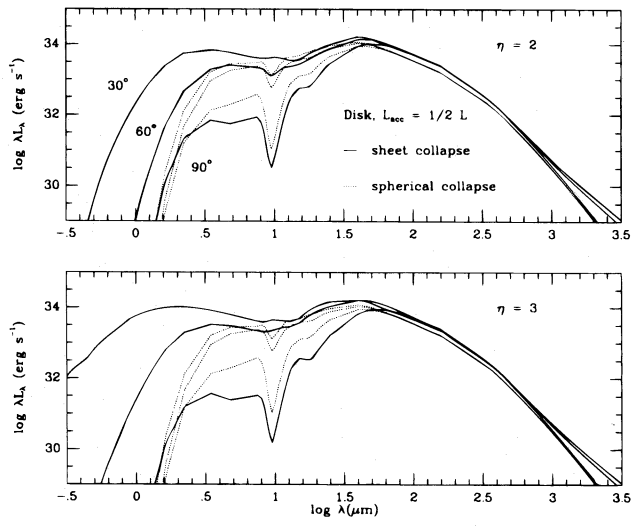

FIG. 6b

FIG. 6.—Spectral energy distributions for η models of Fig. 4 (*heavy solid lines*) compared with a TSC model having the same mass infall rate, central stellar mass, and $R_c = 50$ AU (*light dotted lines*). In descending order of short-wavelength flux, the emission from the models is plotted for inclination angles of $i = 30°$, 60°, and 90°. In (*a*), the central star is the only source of luminosity. In (*b*), a standard, steady, optically thick disk is included, with accretion luminosity equal to half the luminosity of the system.

mean inclination determined for the embedded sources in Taurus using TSC models is substantially lower than the expected average of $i = 60°$ for a random distribution (KCH). The large values of R_c and low inclinations in the TSC models are required to produce a region of reduced extinction around the central object, which allows much more near- and mid-infrared radiation to escape. For some objects, the required large R_c-values imply uncomfortably high rates of rotation in the original cloud, for typical embedded source ages (KCH). In contrast, sheet collapse models can produce near- and mid-infrared fluxes comparable to observations with lower values of R_c and/or higher inclinations, because the flattening is intrinsic and not due to rotation.

As an illustration of how sensitively the derived values of R_c and i depend upon geometry and how flat collapse models can result in smaller centrifugal radii and larger inclinations, consider the similarity of the SEDs shown in Figure 7. Here we show a TSC model with $R_c = 70$ AU and $i = 30°$ and a sheet model with $\eta = 2$ and $R_c = 10$ AU and $i = 50°$. Since the TSC model shown in Figure 7 can reproduce the typical source in Taurus (KCH), but at the price of requiring typically low values of inclination, it follows that the sheet collapse model can similarly explain the observed SEDs in Taurus, with lower values of R_c and more (statistically) plausible inclinations.

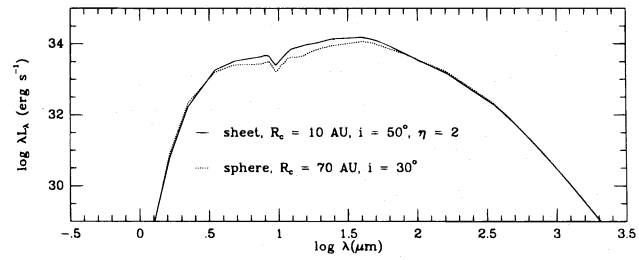

FIG. 7.—Spectral energy distribution of an η model with $R_c = 10$ AU and $i = 50°$ and a TSC model with $R_c = 70$ AU and $i = 30°$, to illustrate the effects of the intrinsic flattening of the sheet collapse.

Yorke et al. (1993) also calculated protostellar spectral energy distributions, and they found that the emergent flux distribution was even more dependent upon inclination than in our models. The difference is apparently due to extinction by the geometrically and optically thick disk of the Yorke et al. calculations, while our disks are geometrically thin. The relevance of the Yorke et al. results to our situation is not clear, because the former assume much higher infall rates and protostellar luminosities than we do (factors of 5–10), as well as much higher initial cloud angular velocities. All of these factors mean that our disks should be much thinner geometrically than those of Yorke et al. and thus less important to the spectral energy distribution. Since Yorke et al. start from initially spherical clouds, their models cannot explain the observed scattered light nebulae that we produce naturally as a result of our collapse cavity.

4. SPECIFIC APPLICATIONS OF SHEET COLLAPSE MODELS

One of the notable successes of star formation theory during the last several years has been the demonstration that TSC infall models can reproduce the main features of the observed spectral energy distributions (SEDs) of the so-called Class I infrared sources (Adams et al. 1987; KCH). These results helped confirm the identification of Class I sources as protostars—i.e., stars that have yet to accrete much of their final mass from an infalling envelope. However, the TSC infall models do not allow enough scattered light to escape at short wavelengths (Adams et al. 1987), and so there must be "holes" or paths of reduced extinction in the dusty envelope to explain the observed near-infrared fluxes (KWGH). Sheet collapse models can in principle help solve this problem, because they combine a CMU (=inner limit of TSC) infall solution with flattened geometry, resulting in reduced extinction along polar directions.

© American Astronomical Society • Provided by the NASA Astrophysics Data System

1996ApJ...464..387H

The issue of holes in infalling envelopes is even more crucial to understanding the so-called "flat spectrum" T Tauri stars. Calvet et al. (1994) showed that the far-infrared emission of these objects is very likely the result of thermal emission from an infalling dusty envelope having essentially identical properties to those of Class I sources in Taurus. This explanation requires a large envelope hole situated at a favorable inclination to explain the large amount of scattered optical light observed in flat spectrum sources. The sheet collapse model, with large evacuated cavities and dusty equatorial infalling material, can potentially provide the required emission at both short and long wavelengths. Moreover, radio-wavelength observations of the archetypal flat-spectrum source HL Tau suggest that the infalling material is flattened in geometry (Hayashi et al. 1993).

In the following sections we discuss more specific applications of the sheet collapse picture to heavily embedded young stellar objects.

4.1. *Class I Sources: IRAS 04016+2610*

We first consider IRAS 04016+2610, which is a fairly typical Taurus Class I source (KCH). The values of $\dot{M}$ and R_c derived from fitting the SED (for an assumed central mass of 0.5 $M_\odot$) are similar to that predicted by theory for Taurus (Shu 1977; Adams et al. 1987; KCH). However, 04016+2610 exhibits much more near-infrared emission than can be explained by a TSC infall model. There must be a path of lower extinction through the envelope than predicted by the TSC model. There is direct evidence for this low-extinction region in the observed extended near-infrared image. The scattered light nebula appears to be roughly conical with a large opening angle (KWGH).

In Figure 8 we compare the SED for this object with calculations for a model with $\eta = 2$, which produces a reflection nebula with a substantial opening angle (Fig. 5). The adopted inclination, ρ_1, and envelope outer radius (3000 AU) are the same as those in KCH, KWGH for this source; R_c has been decreased from 70 AU to 50 AU. The agreement is quite good, showing that the large opening angle sheet collapse model fits well. Thus, an $\eta = 2$ model results in a good fit to the SED of 04016+2610 and can explain the relatively wide opening angle of the scattered light nebula (compare Fig. 13 of KWGH to Fig. 5).

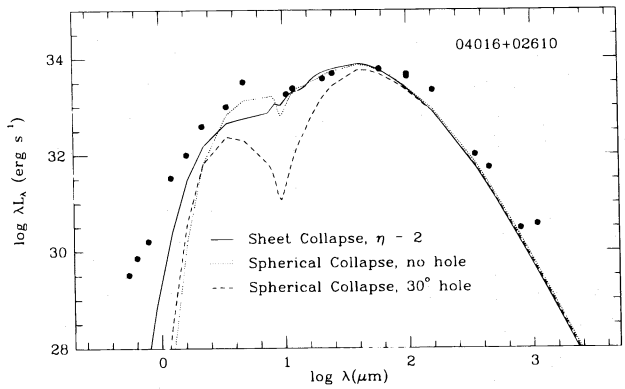

FIG. 8.—Spectral energy distribution of the Class I Taurus source IRAS 04016+2610 (Kenyon et al. 1993a), compared with a flattened collapse model with $\eta = 2$, $i = 60°$, and $R_c = 50$ AU (*solid line*). The dotted line shows a TSC model without a hole that reproduces the observed SED, from Kenyon et al. (1993a). The dashed line shows this same model, but with a hole of opening angle $\sim 30^{\rm circ}$, which reproduces the observed image (Kenyon et al. 1993b; see text).

It is instructive to compare these results with those obtained with modified TSC models, in which the envelope cavities are produced by outflows having streamline cavities with wide opening angles (§ 3.1). We assume that the outflow completely evacuates the envelope within an angle θ_w of the axis of symmetry (e.g., Calvet et al. 1994). The dotted line in Figure 8 shows the TSC model that fits the SED of 04016+2610, without a hole. The dashed line shows the SED of a modified TSC model with $\theta_w = 30°$, which is a minimum opening angle necessary to reproduce the morphology of the near-infrared reflection nebula of 04016+2610. The resulting SED has two very pronounced peaks with a very large reduction of flux at $\lambda \lesssim 30$ μm. The mid-infrared emission disappears because the outflow removes all of the low-angular momentum infalling matter, which is the only material that can come close to the star. In the rotating CMU infall model, the closest that infalling dust would come to the central star is

$$R_{\rm min} = R_c \sin^2 \theta_w . \qquad (12)$$

For example, if $\theta_w = 30°$, then $R_{\rm min} = 0.25 R_c$. Thus, a hole of this opening angle removes the low-angular momentum material landing interior to ~ 18 AU. This implies that the dusty envelope gets no hotter than about 100 K (Calvet et al. 1994), which in turn results in a pronounced drop in envelope emission shortward of $\lambda \sim 30$ μm and results in an unacceptable fit to the observed SED. In contrast, the sheet model reduces, but does not completely eliminate, the infalling dust at small scales, improving the match between predicted and observed SEDs.

The simple model of an outflow hole assumes that the wind is strictly limited to a cone of constant opening angle and that there is no nonradial transfer of momentum between outflow and envelope. However, it is difficult to imagine any interaction between a bipolar outflow and an infalling envelope that would not deflect the outflow toward the axis of symmetry and therefore deflect the infall away from the radial direction. This would cause the infalling matter to land on the disk at larger radii than given by equation (9), making the SED problem worse.

In principle, a dusty wind could help fill in the cavity (e.g., Königl 1989). Since the wind has a very different density distribution than the infall, it is not clear whether such a model could actually explain the observed SEDs, and whether the required mass-loss rates are present. In any event, since there are reasons to question whether wide-angle outflows exist, dusty or not (e.g., Masson & Chernin 1993), it is suggestive that the flat collapse model can produce scattered-light cavities with opening angles on small scales ($\lesssim 10^3$ AU) that are much wider than typical jets, and that this model can reconcile the SEDs with the reflection nebula morphologies without requiring a dusty, wide-angle outflow.

4.2. *Class I Sources: General Implications*

We next consider the general differences that the adoption of flattened infall models would make in our previous estimates of physical parameters for the Taurus Class I sources (KCH). Figures 6–8 indicate that, for typical parameters of Taurus Class I sources, the flattening of the initial envelope does not affect the position of the peak of

© American Astronomical Society • Provided by the NASA Astrophysics Data System

1996ApJ...464..387H

the spectral energy distribution very much (unless the central star becomes optically visible). Because the far-infrared emission arises from optically thin regions, the observed flux is relatively insensitive to geometry for a given total emitting mass at the same temperature. Our method of determining radiative equilibrium temperatures results in very similar temperature distributions in the envelope exterior to R_c for both TSC and sheet collapse models with the same $\dot{M}$, and therefore it is not surprising that the peak of the SED does not change wavelength significantly as a function of η. However, we must caution that this result depends critically on the assumption of the spherical temperature distribution. In general, we expect envelope temperatures to be highest in the polar directions and lowest in equatorial regions, where most of the emitting mass resides (e.g., Chick et al. 1996). A proper treatment of radiative equilibrium might indicate a shift of the SED peak to longer wavelengths because of the lower temperatures, which in turn might mimic a higher $\rho_1 \propto \dot{M} M^{-1/2}$. This issue needs further exploration.

Values of R_c and inclination i to the line of sight estimated from SEDs are likely to change significantly with the adoption of a sheet collapse model, as already discussed in the context of 04016+2610. The line-of-sight extinction toward the central regions,

$$\tau_r(i) \propto f(i) \dot{M} (M R_c)^{-1/2} , \quad (13)$$

is the principal factor controlling the amount of near- and mid-infrared light escaping from the envelope. Here $f(i)$ incorporates the angle-dependence of the density distribution, which varies by roughly a factor of 2 for CMU/TSC models. For TSC models, the polar optical depth is roughly a factor of 2 smaller than the nearly equator-on optical depth; the variation is much larger for sheet models.

It is evident from Figure 2 that, for a typical value of $\eta \sim 3$, and for the same $\dot{M}$ and R_c, a sheet model will have a substantially smaller $\tau_r(i)$ than the corresponding TSC model over a large range of inclination angles, $\cos i \sim \mu_0 \gtrsim 0.3$. This result is interesting because SED modeling using TSC density distributions often indicate implausibly low inclinations, which are needed to reduce the near- to mid-infrared extinction. For example, KCH found that 13 of the 21 Taurus Class I sources surveyed required TSC models with $i = 30°$ or $i = 10°$, which is inconsistent with a random distribution of inclinations. As shown by KWGH, dusty envelopes with "holes" can fit the data with larger inclinations. Sheet collapse models, which provide much more evacuated polar cavities than TSC models, can fit the data at larger, more plausible inclinations. If the inclination is fixed, then the sheet model will require a much smaller value of R_c to have the same extinction as the corresponding TSC model. The results of KCH showed a correlation between R_c and $\dot{M}$, in the sense that sources with higher infall rates tended to require larger centrifugal radii. The observational result that requires this correlation is that objects with large estimated infall rates, as indicated by their very red far-infrared spectra, still tend to exhibit significant amounts of near- and mid- infrared light. Adoption of flattened collapse models could eliminate this apparent correlation. For example, an $\eta = 3$ model with the same infall rate will have less than half the line-of-sight extinction to the central star at $i = 60°$ as the equivalent CMU/TSC model, implying that the centrifugal radius could be more than *4 times* smaller. Given this sensitivity of derived parameters to geometry, SED estimates of R_c must be regarded as very uncertain.

For nearly equator-on sources, sheet models will exhibit larger $\tau_r(i)$ than the corresponding TSC model. The larger extinction may play a role in helping explain very red sources, although modeling the SEDs of "Class 0" sources (Andre et al. 1993) may also require higher infall rates, an issue we shall address in a subsequent paper. In this context, it is worth noting that our isothermal sheet collapse model is characterized by a higher mass infall rate than the TSC collapse would exhibit for the same cloud temperature (§ 2).

4.3. *Flat Spectrum Sources: HL Tau*

As another example of how sheet infall models can eliminate the discrepancy between SED fitting and the reflection nebula morphology, as well as explain other observational features, we consider an application to the flat spectrum T Tauri star HL Tau (Adams et al. 1988). This optically visible object has a very large infrared excess, so that the SED is relatively flat between about 3 and 100 μm. Calvet et al. (1994) showed that the mid- to far-infrared emission of HL Tau could be reproduced by infalling envelope models with typical parameters of Class I stars in Taurus; in particular, the SEDs of 04016+2610 and HL Tau are very similar. The infall rate needed to explain the far-infrared emission is also consistent with analyses of near-infrared scattered light by Beckwith et al. (1989), redshifted C_2 absorption (Grasdalen et al. 1989), and ^{13}CO radio interferometer maps (Hayashi et al. 1993; see below). However, as in the case of 04016+2610, the Calvet et al. envelope model for the SED HL Tau was unsatisfactory in that it demanded a narrow polar envelope hole, with a half-angle $\sim 10°$. In contrast, the observed optical nebula has a quite large apparent opening half-angle, $\approx 45°$ (e.g., Gledhill & Scarrott 1989; Stapelfeldt et al. 1995), but a cavity model with a streamline hole, adopting an opening angle of this magnitude, would result in an unacceptable fit to the SED (see Fig. 8; see also Fig. 6 of Calvet et al. 1994).

In this subsection, we consider in turn how well sheet collapse models explain the SED of HL Tau, its scattered light image, and its near-infrared polarization and photocenter shift with wavelength. Our constraints are (1) an infall rate comparable to that derived by Hayashi et al. (1993) from independent analysis of the ^{13}CO interferometer maps, and (2) a centrifugal radius R_c smaller than the ~ 140 AU outer disk radius suggested by the sub-mm interferometry of Lay et al. (1994). (We expect that the disk, if anything, will have spread to larger radii than R_c; CM). The first constraint is straightforwardly met, since we assume $\dot{M} = 4 \times 10^{-6}\ M_\odot\ \mathrm{yr}^{-1}$, the typical mean value of infall rates found for Taurus Class I sources by Kenyon et al. (1993a), essentially equal to the infall rate derived by Hayashi et al. (1993), and sufficiently close to the $\dot{M} \sim 6 \times 10^{-6}\ M_\odot\ \mathrm{yr}^{-1}$ we found for the "plateau" phase of infall in our isothermal numerical simulation. We also adopt $R_c = 50$ AU for concreteness, although the precise value adopted is not critical given the sensitivity of the results to inclination (§ 4.2). Finally, since HL Tau is apparently surrounded by an envelope with a mass accretion rate comparable to that observed and predicted for the main infall phase, we might expect "intermediate" values of $\eta \sim 2$–3.

Figure 9 compares SEDs calculated for sheet collapse models with $\eta = 2$, 3 to the observed SED of HL Tau. The

© American Astronomical Society • Provided by the NASA Astrophysics Data System

1996ApJ...464..387H

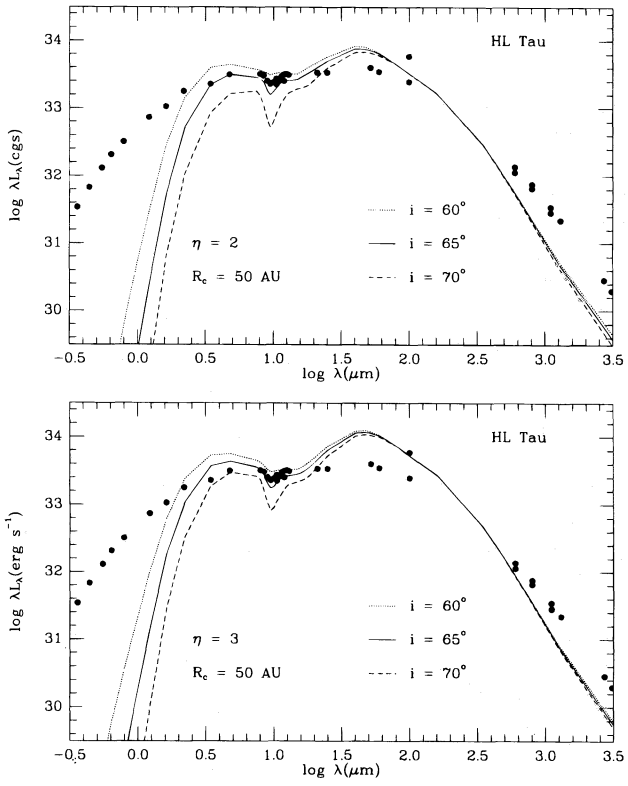

FIG. 9.—Spectral energy distribution of the flat-spectrum T Tauri star HL Tau (Calvet et al. 1994), compared with flattened collapse models with $\eta = 2$, 3 and $R_c = 50$ AU (see text).

$\eta = 2$ model fits the long-wavelength infrared emission better than the $\eta = 3$ model, which exhibits too much flux. Once again we emphasize that our assumption of a spherical temperature distribution may cause the comparison with the $\eta = 3$ model to appear worse than it actually should. In a more accurate radiative equilibrium calculation, the polar, low-density regions will be hotter because radiation will preferentially escape in these directions; the equatorial, densest regions, will become cooler. Since the far-infrared emission comes from optically thin regions, and most of the emitting envelope in a sheet model is in the equatorial region, a sheet model would probably have lower temperatures and therefore lower far-infrared fluxes. This conjecture is supported by the modeling of Chick et al. (1996), who considered infalling envelopes with cavities; using a Rosseland mean opacity, Chick et al. found that the equatorial envelope temperatures could be as much as a factor of 2 lower than the spherical case for large cavities, such as implicit in the $\eta = 3$ model.

We also note that the depth of the 10 μm silicate feature is very sensitive to the system inclination. In both models the best comparisons occur for $i \sim 65°$, or $\mu \sim 0.4$. Our models show that the silicate feature depth is so geometry-dependent that it is unlikely to be a reliable measure of envelope optical depth.

Figure 10 shows scattered light images for the $\eta = 2$, 3 models at appropriate inclinations. From Table 1 it can be seen that the observed HL Tau J-band polarization (10%, Hodapp 1984) can be roughly reproduced at $\eta = 2$ if $\mu = 0.5$ or at $\eta = 3$ if $\mu = 0.3$. The true system inclination is unknown, but the aspect ratio of the molecular gas observed by Sargent & Beckwith (1991) and Hayashi et al. (1993) suggests $\mu \approx 0.5$. The appearance of the large-scale scattered light nebula is perhaps better matched by $\eta = 3$ models, which provide reasonable agreement with the wide opening angle suggested by large-scale images, although the *HST* images show fine-scale structure in the nebula (Stapelfeldt et al. 1995) that cannot possibly be explained by the simple axisymmetric model used here.

The Calvet et al. TSC model for HL Tau demanded a narrow outflow hole, because an evacuated hole with a wide opening angle eliminates the mid-infrared excess as discussed above (see also Fig. 6 of Calvet et al. 1994). With such a narrow cavity, the reflection nebula morphology would look quite different than observed. The η models do not have the same problem because the envelope cavity is not completely evacuated of dust; even small amounts of material can provide the required mid-infrared emission.

Beckwith & Birk (1995) showed that the position of the peak near-infrared intensity in HL Tau shifts in position by about $0\farcs53 \pm 0\farcs07$ ~74 AU between 2.12 and 1.25 μm; this result was confirmed and extended in wavelength by Weintraub, Kastner, & Whitney (1995). Both sets of authors interpret this shift as due to a combination of an extended scattered light nebula seen behind a medium with an extinction gradient. Beckwith & Birk suggested that the extincting medium might be either an infalling envelope or the extended atmosphere of a circumstellar disk; Weintraub et al. favored the former explanation.

Our models also predict photocenter shifts, since the central star is hidden by a scattering, absorbing envelope with a substantial spatial gradient in its column density. We convolved the models with a 1″ Gaussian point spread function to be more directly comparable to the ground-based measurements. For $\eta = 2$, we find shifts at J of 16 AU and 53 AU at $\mu = 0.5$ and $\mu = 0.4$, respectively; for $\eta = 3$, the shifts at J are 10 and 63 AU at $\mu = 0.4$ and $\mu = 0.3$, respectively. The two largest of these shifts are reasonably consistent with the observations, although the polarizations predicted by the large photocenter shift models, 11% and 19% (see Table 1), are somewhat larger than observed.

Two other observations are more difficult to explain with our models. First, Beckwith & Birk (1995) find a decrease of intensity with radial distance $\propto r^{-4}$ in the cleaned J image of HL Tau between about $1\farcs2$ and $3\farcs5$ ~170–490 AU) from the position of peak intensity. As Beckwith & Birk discuss, this dependence of intensity on radius is much steeper than predicted by infall models. Second, the model parameters that explain the photocenter shifts and polarizations predict that only $\lesssim 1\%$ of the light from the central object is observed at J, while the observations suggest that more light is detected. HL Tau is observed to be relatively bright at J; given the system luminosity $\sim 5\ L_\odot$, and various assumptions about the temperature or intrinsic SED of the central source, the observations suggest that something like 5%–10% of the intrinsic emitted J flux is visible as scattered light.

These difficulties with our models, in addition to the modest discrepancies between best fits for SEDs and scattered light properties, may be attributable to the complex structure of the real scattered light nebula, as seen in the *HST* images at 0.555 and 0.814 μm (Stapelfeldt et al. 1995). The *HST* observations indicate a "C"-shaped bright structure, with a diameter $\sim 1\farcs2$ ~170 AU, extending a comparable distance in extent in the direction of the jet from the estimated stellar position. This extremely complex structure

© American Astronomical Society • Provided by the NASA Astrophysics Data System

1996ApJ...464..387H

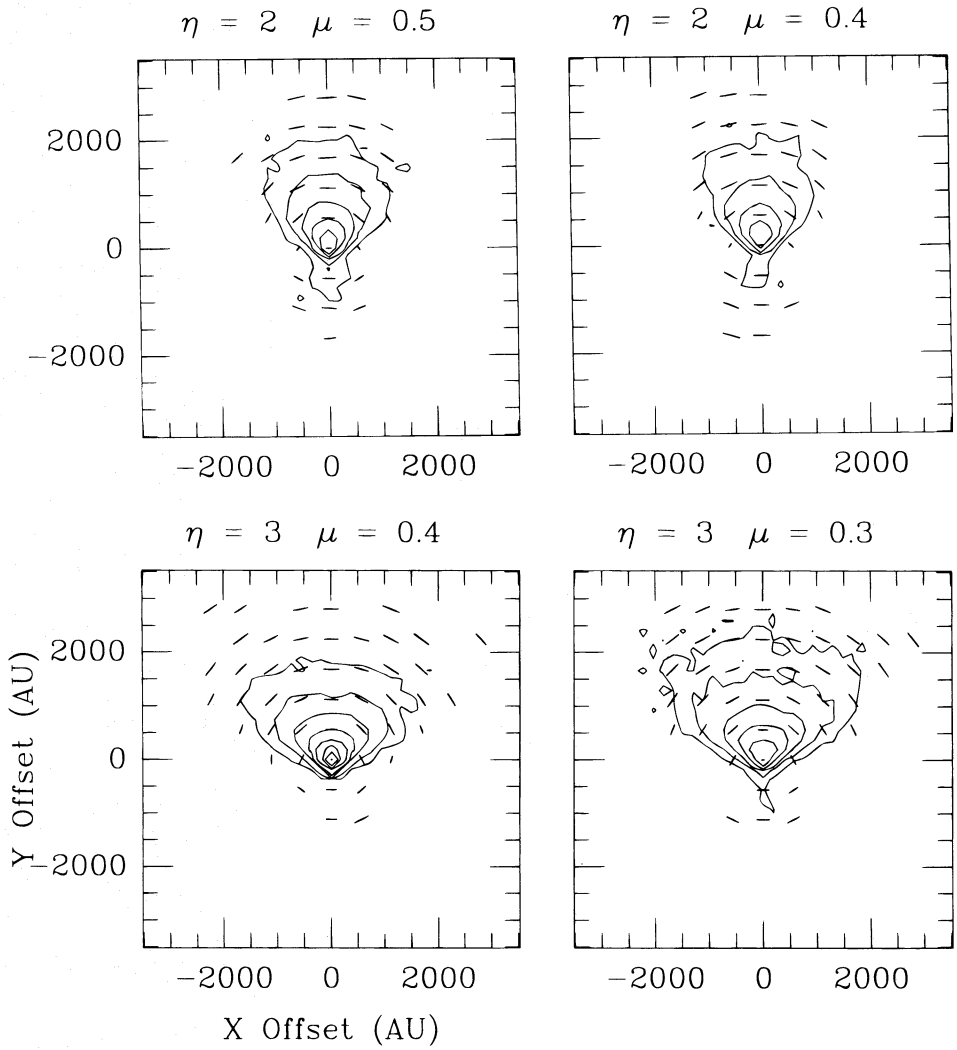

FIG. 10.—Scattered light calculations at $\lambda = 1.25$ μm for $\eta = 2, 3$, each at two inclinations, for the HL Tau models (see Fig. 9, text)

is not predicted by any simple axisymmetric infall or disk model and may be responsible for the departure of the observed surface brightness gradients in the nebula from the predictions of simple infall models. The models predict visual extinctions of several magnitudes through the envelope in this region, so relatively small fluctuations in the column density could produce large effects in the optical and J-band surface brightness distributions, photocenter shifts, and polarizations.

Perhaps more important, the *HST* scattered-light images do not show structure obviously related to the jet, in the sense that the cavity might have closely bounded the outer limits of the jet. The relationship, if any, of the bright "C" feature to the outflow is unclear. The full opening angle of the scattered light nebula observed with *HST* is $\gtrsim 90°$, and would therefore require an essentially uncollimated outflow to produce this structure, while the observed jet is highly collimated (Mundt, Ray, & Bührke 1988).

Hayashi et al. (1993) argued that the motions of the circumstellar envelope of HL Tau, observed with the Nobeyama Millimeter Array in the ^{13}CO $J = 1$–0 line, were consistent with a gas disk falling in at a rate $\sim 5 \times 10^{-6}$ $M_\odot$ yr^{-1} (see also Lin et al. 1994). We have computed crude velocity channel maps to provide an initial comparison with the Hayashi et al. results, by assuming that the emission is optically thin and nearly isothermal, so that we may substitute the column density through the envelope in a given velocity range for the actual ^{13}CO line emission. As shown in Figure 11, the column density channel maps for $\eta = 3$ are qualitatively similar to the velocity patterns seen in the map of Hayashi et al. The channel map patterns exhibited in Figure 11 are essentially the same as those calculated by Koerner & Sargent (1995b) for a geometrically thin infalling and rotating disk.

In summary, we find that flattened infall models can explain the main features of the SED, the polarization, the photocenter shifts with wavelength, and the molecular gas velocity patterns of HL Tau. The quantitative agreement with most of the observations is fairly good, considering the true complexity of the nebular geometry, which we can only approximate with our simple models.

5. DISCUSSION

Our principal result is that flattened dusty protostellar envelopes will collapse to form cavities that greatly enhance the escape of short-wavelength radiation. Because initial spherical symmetry is an unlikely initial condition, such collapse cavities should be a general phenomenon. The amplification of flattening during collapse suggests that more spherical protostellar clouds than assumed here still

© American Astronomical Society • Provided by the NASA Astrophysics Data System

1996ApJ...464..387H

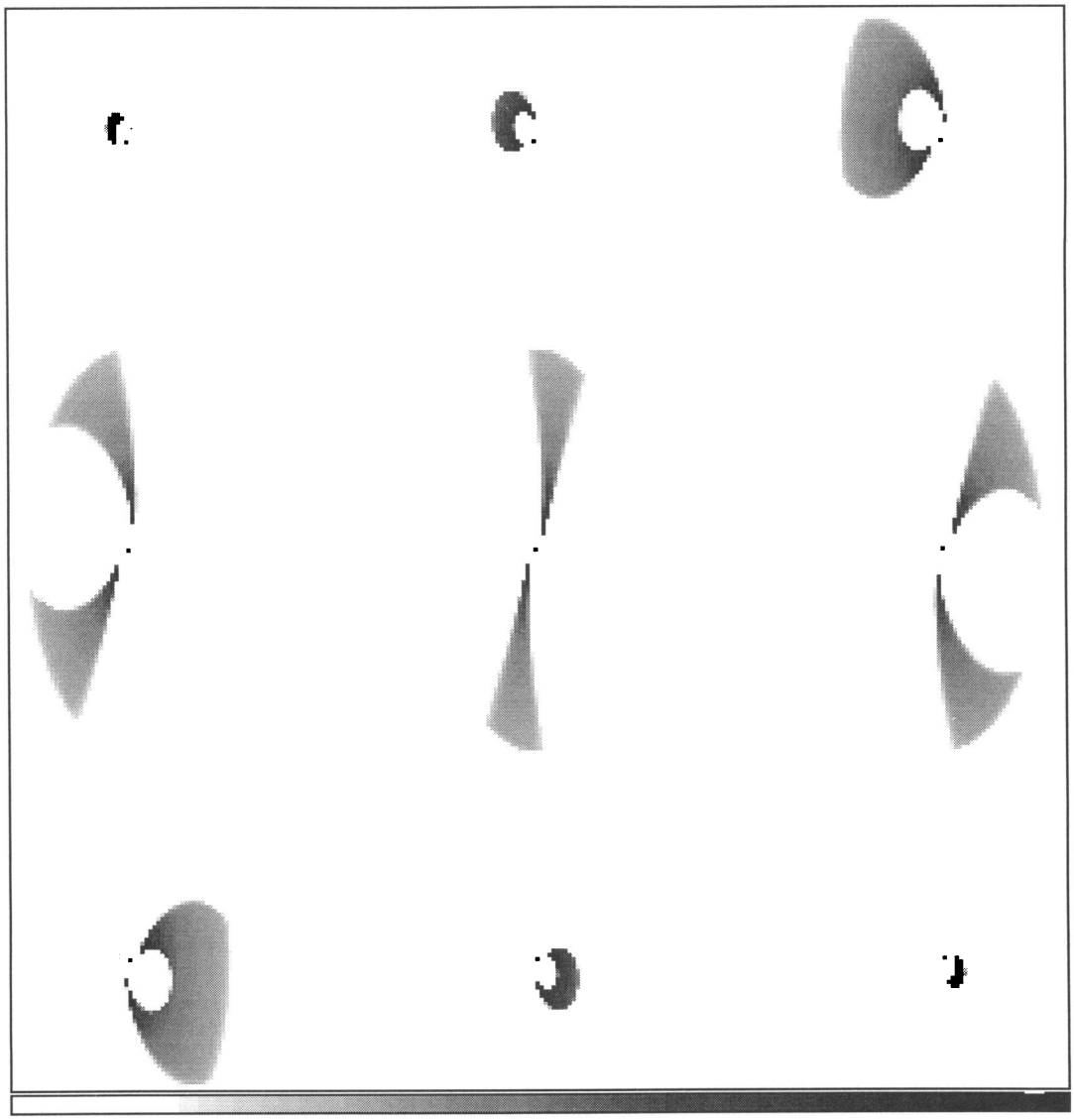

FIG. 11.—Column density velocity channel maps for the $\eta = 3$, observed at an inclination of 60°. The linear gray scale indicates column densities; the projected major axis of the envelope is vertical. The outer radius of the envelope is 10 times R_c. Each channel map is separated by 0.5 km s^{-1} for $R_c = 100$ AU, with a central mass of 0.5 $M_\odot$.

may exhibit important observational effects due to the initial geometry, particularly in later stages of collapse.

5.1. *Disks versus Flattened Infall*

Interferometric maps in both radio-wavelength lines and continua have been made of many young stellar objects in recent years (e.g., Sargent & Beckwith 1991; Hayashi et al. 1993; Koerner & Sargent 1995a; Ohashi & Hayashi 1995). In a number of cases, dust or gas structures with size scales $\approx$1000 AU have been discovered and interpreted as disks with masses $\sim 10^{-2}$–10^{-1} $M_\odot$. However, the interpretation of these structures as rotationally supported circumstellar disks is often difficult to support conclusively, as the case of HL Tau shows. In HL Tau, it appears that the $\sim$1000 AU structure is falling in, while a more compact structure $\sim$60 AU in size, observed at sub-mm wavelengths (Lay et al. 1994), may be the Keplerian disk. This distinction between infall on large scales and rotation on small scales makes sense in terms of typical angular velocities observed in Taurus molecular clouds (Goodman et al. 1993), which suggest that the angular momentum barrier may not generally be important on scales of thousands of AU. Since the spatial resolution of many maps is typically a few arcsec or a few hundred AU, the true Keplerian disks of many young stellar objects may be unresolved.

Beyond these considerations, our model of flattened collapse suggests that infalling envelopes may well appear to look like toroids or disks even when they are not rotationally supported, making it more difficult to distinguish between disks and sheet collapse. As Figure 12 shows, our numerical simulation of sheet collapse, observed at an intermediate stage, exhibits a mass of $\sim$0.03 $M_\odot$ at a radius of 1000 AU or $\log r/r_{\rm out} = -0.75$. Similar "disk" masses on these size have been observed by a number of authors (Ohashi & Hayashi 1995; Osterloh & Beckwith 1995). Clearly, further investigation of the issue of disk vs. envelope dust mass is warranted, especially for objects with large far-infrared excesses most easily explained by thermal dust emission from infalling envelopes (Calvet et al. 1994).

Analyses of interferometric maps often implicitly depend upon the assumption that the envelope is more or less axisymmetric. For example, Hayashi et al. (1993) assumed

© American Astronomical Society • Provided by the NASA Astrophysics Data System

1996ApJ...464..387H

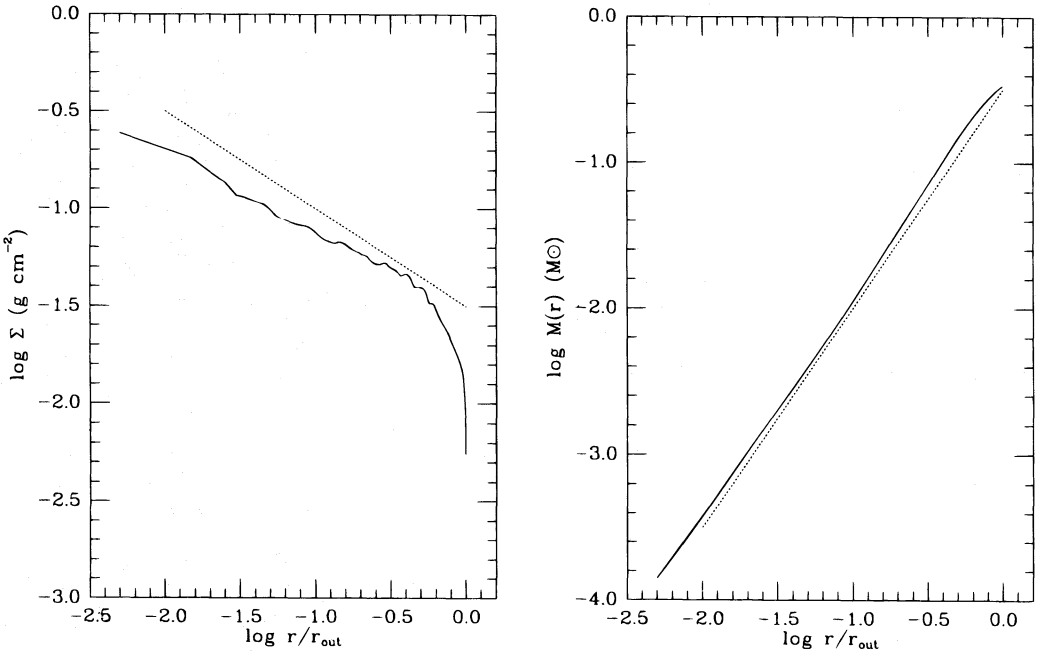

FIG. 12.—Surface density distribution and enclosed mass as a function of cylindrical radius for the numerical simulation after about $\frac{2}{3}$ of the final mass has been accreted into the central object (lower left model shown in Fig. 1). The outer radius is $r_{out} = 8.6 \times 10^{16}$ cm $= 5.7 \times 10^3$ AU. The dashed lines correspond to power laws $\Sigma \propto r^{-1/2}$ and $M(r) \propto r^{3/2}$. The power laws correspond to the predicted behavior for spherical collapse; the flat collapse simulation exhibits similar behavior when viewed from the axis of symmetry.

that the gas distributed around HL Tau is intrinsically circularly symmetric, but appears flattened on the sky due to the inclination of the system; this assumption makes it possible to argue which portion of the minor axis is on the "far" side of the star, which is necessary to distinguish infall from outflow. If the envelope is actually filamentary, as suggested by some simulations of fragmentation, the projected structure on the sky could be quite complex and difficult to interpret.

5.2. *The Pseudodisk versus the Sheet Model*

Galli & Shu (1993a, 1993b) pointed out that even a modest magnetic field structure could deflect infall from an initially spherical cloud to form a "pseudodisk", i.e., a flat thin structure in the equatorial plane that was not rotationally supported and therefore falls in. This thin pseudodisk is surrounded by an infalling envelope whose density distribution does not initially depart that much from the TSC solution. As the collapse proceeds, the numerical calculations show a tendency for the outer density contours of the infalling envelope to flatten much more than in a TSC model. It could be difficult to distinguish fairly flattened sheet models from pseudodisk structures in radio interferometer maps (e.g., § 4.3; Fig. 11), especially if the interferometry resolves out the large-scale envelope structure.

However, in contrast to our models, the Galli & Shu (1993b) numerical calculations show a tendency for material to pile up near the axis of symmetry while we obtain a cavity. Thus, the pseudodisk model by itself would not provide an explanation for the envelope holes needed to explain the observed scattered light at short wavelengths. The sheet models provide a natural explanation of this nebular morphology, where the Galli & Shu models do not.

We suggest that a more general result would be a structure with both a thin pseudodisk in the equatorial plane as well as a flattened toroidal infalling envelope structure, such as that found by Nakamura et al. (1995). The cavities resulting from initial geometry are needed to explain the observed morphologies of scattered light nebulae, and would be expected to develop since the initial cloud, threaded by the magnetic field, cannot be strictly spherically symmetric in hydrostatic equilibrium anyway (e.g., Mouschovias 1976). Whether the very flat pseudodisk can be distinguished observationally from the moderately flattened infalling envelope will depend to some extent upon initial geometry of the cloud and how far the collapse has proceeded. As shown in § 4.3, it can be difficult to distinguish between a relatively flattened toroidal collapse and a true pseudodisk with velocity channel maps.

5.3. *Bipolar Cavities and Outflows*

In the sheet collapse picture, at least part of the reflection nebula cavity can be the result of collapse rather than outflow. Why then are reflection nebula cavities apparently often aligned with outflows? Here we must differentiate cases on the basis of size. On *large* scales (>0.1 pc), typical of many outflows, ambient material may not even be bound to the exciting star; in any the collapse time on these scales for a low-mass star would be longer than the outflow timescale, and so the cavity development during collapse discussed in this paper cannot operate. Therefore, the structure of the reflection nebulae on such large scales must reflect either the outflow geometry, as we assumed in previous work (e.g., Whitney & Hartmann 1993), or the ambient medium structure, or both. For example, in L1551 IRS 5, the reflection nebula has its greatest extent ~ 0.5 pc from the source, which is too far for collapse motions to be relevant. We note, however, that the position angle of the jet is near, but not at, the midpoint of the opening angle of the scattered light nebula close to the source (Davis, Mundt, & Eisloeffel 1995).

On *small scales* ($\lesssim 10^3$ AU), collapse motions can make a difference during the lifetime of the outflow/embedded

© American Astronomical Society • Provided by the NASA Astrophysics Data System

1996ApJ...464..387H

phase, and our sheet collapse model for reflection nebulae becomes relevant. We have suggested that large opening angle nebulae like HL Tau's may be most easily explained using the sheet collapse, given that the outflow jet in HL Tau appears to be highly collimated (e.g., Mundt et al. 1988). Studies of jets suggest that they are highly collimated on such small scales, especially in the youngest phases of evolution (e.g., Kepner et al. 1993). The SED problem of § 4.1 can be avoided if the jets or outflows have half-opening angles $\lesssim 10°$, or full opening angles of $\lesssim 20°$, assuming reasonable angular momenta of the infalling cloud (see Calvet et al. 1994). There may be mechanisms by which outflows can become wider at larger distances; for the present models, we require only that the outflows be narrow on small scales.

Much less is known about the orientation of dense material on small scales relative to outflows. Observations may require some alignment between the large-scale flat sheet structure and the jet/outflow axis, such as appears to occur in HL Tau (e.g., Sargent & Beckwith 1991; Hayashi et al. 1993); further investigation of this question is needed. We speculate that the magnetic field may provide a large-scale mechanism to correlate the overall flattening of the envelope with its rotation axis, even though rotation is not dynamically important on large scales. The gas cloud will tend to flatten preferentially in a direction perpendicular to the restraining magnetic fields (Mouschovias 1976); and, because magnetic braking is more efficient for angular momentum vectors perpendicular to the field lines (see Mouschovias 1991), one might expect the resulting cloud to preferentially have its angular momentum perpendicular to the overall cloud flattening. This would imply a combination of the Galli-Shu magnetic collapse model with an initially flattened density structure similar to that investigated here.

5.4. *Complications and Triggered Collapse*

If fragmentation of protostellar clouds into binary or multiple systems is the norm, it would be highly surprising if infalling envelopes were really axisymmetric. We have assumed so in this work for simplicity and because of the computing demands of the radiative transfer calculations. Triaxial geometries for infalling envelopes may play an important role in explaining many binary objects, in which the primary is optically visible, while the secondary is heavily enshrouded by dust and only detectable in the infrared (e.g., Ghez, Neugebauer, & Matthews 1993; Leinert et al. 1993). To explain these objects, one requires an extinction distribution that is highly structured on scales ~ 100 AU or less, and a filamentary or prolate collapse structure might result in many more evacuated lines of sight for an infalling envelope than our simple axisymmetric model. In addition, one can contemplate more general cases than we have treated, in which the rotation axis is not perfectly aligned perpendicular to the sheet plane, which would also lead to much more complicated patterns of extinction.

Finally, it is increasingly clear that many low-mass stars form in quite close proximity to high-mass stars with strong ionizing fluxes and powerful winds (e.g., Zinnecker et al. 1993). In such circumstances one could imagine that pressure waves driven by central massive stars in a dense cluster could be responsible for triggering some star formation. Even if the protostellar cloud shocked in this way is initially spherical, the ram pressure of the shock wave flattens the cloud into a compressed parabolic shell that can undergo self-gravitational collapse (Boss 1995). If the initial cloud is somewhat flattened, the response to a triggering impulse from the right direction would be to produce an even more flattened structure. In either case, our model of protostellar collapse from a sheet might well be relevant.

6. CONCLUSIONS

We have shown that gravitational collapse of an initially flattened protostellar cloud naturally produces cavities in the dusty infalling envelope qualitatively similar to the envelope cavities inferred from scattered light observations of young stellar objects. Axisymmetric models suggest that a toroidal structure will be produced from collapse of a sheet, resulting in a flattened distribution of gas and dust that looks like a flared disk on large scales. Departures from sphericity in the initial protostellar cloud are likely to be common and should be considered in interpreting the collapsing envelopes of young stellar objects.

We are grateful to Barbara Whitney for her assistance in using the Monte Carlo scattering code. We also thank John Tsai for communicating the scaling argument for the mass infall rate presented in § 2. This work was supported in part by NASA grant NAGW-2306, NSF grant AST 90-23554, and STScI grant GO-5355.01.93A. A. P. B. was partially supported by NSF grant AST 92-17967.

REFERENCES

Adams, F. C., Lada, C. J., & Shu, F. H. 1987, ApJ, 312, 788
———. 1988, ApJ, 326, 865
Adams, F. C., & Shu, F. H. 1986, ApJ, 308, 836
Andre, P., Ward-Thompson, D., & Barsony, M. 1993, ApJ, 406, 122
Appenzeller, I., & Tscharnuter, W. 1974, A&A, 30, 423
Beckwith, S. V. W., & Birk, C. C. 1995, ApJ, 449, L59
Beckwith, S. V. W., Sargent, A. I., Koresko, C. D., & Weintraub, D. A. 1989, ApJ, 343, 393
Bodenheimer, P., & Black, D. C. 1978, in Protostars and Planets, ed. T. Gehrels (Tucson: Univ. Arizona Press), 288
Bonnell, I., & Bastien, P. 1992, ApJ, 401, 654
Boss, A. P. 1980, ApJ, 237, 563
———. 1993, ApJ, 410, 157
———. 1995, ApJ, 439, 224
Boss, A. P., & Myhill, E. A. 1992, ApJS, 83, 311
Butner, H. M., Evans, N. J., II, Lester, D. F., Levreault, R. M., & Strom, S. E. 1991, ApJ, 376, 676
Butner, H. M., Natta, A., & Evans, N. J., II. 1994, ApJ, 420, 326
Calvet, N., Hartmann, L., Kenyon, S., & Whitney, B. 1994, ApJ, 434, 330
Cassen, P., & Moosman, A. 1981, Icarus, 48, 353 (CM)
Chick, K. M., Pollack, J. B., & Cassen, P. 1996, ApJ, 461, in press
Davis, C. J., Mundt, R., & Eisloeffel, J. 1995, Ap&SS, 224, 121
Efstathiou, A., & Rowan-Robinson, M. 1991, MNRAS, 252, 528
Galli, D., & Shu, F. H. 1993a, ApJ, 417, 220
———. 1993b, ApJ, 417, 243
Ghez, A., Neugebauer, G., & Matthews, K. 1993, AJ, 106, 2005
Gledhill, T. M., & Scarrott, S. M. 1989, MNRAS, 236, 139
Goodman, A. A., Benson, P. J., Fuller, G. A., & Myers, P. C. 1993, ApJ, 406, 528
Grasdalen, G. L., Sloan, G., Stout, M., Strom, S. E., & Welty, A. D. 1989, ApJ, 339, L37
Hartmann, L., Boss, A. P., Calvet, N., & Whitney, B. 1994, ApJ, 430, L49 (Paper I)
Hayashi, M., Ohashi, N., & Miyama, S. 1993, ApJ, 418, L71
Hodapp, K.-W. 1984, A&A, 141, 255
Kenyon, S. J., Calvet, N., & Hartmann, L. 1993a, ApJ, 414, 676 (KCH)
Kenyon, S. J., & Hartmann, L. 1987, ApJ, 323, 714
Kenyon, S. J., Whitney, B., Gomez, M., & Hartmann, L. 1993b, ApJ, 414, 773 (KWGH)
Kepner, J., Hartigan, P., Yang, C., & Strom, S. 1993, ApJ, 415, L119
Koerner, D. W., & Sargent, A. I. 1995a, AJ, 109, 2138
———. 1995b, Ap&SS, 223, 169
Königl, A. 1989, ApJ, 342, 208
Larson, R. B. 1972, MNRAS, 157, 121

© American Astronomical Society • Provided by the NASA Astrophysics Data System

1996ApJ...464..387H

Larson, R. B. 1985, MNRAS, 214, 379
Lay, O. P., Carlstron, J. E., Hills, R. E., & Phillips, T. G. 1994, ApJ, 434, L75
Lazareff, B., Pudritz, R. E., & Monin, L.-L. 1990, ApJ, 358, 170
Leinert, C., Zinnecker, H., Christou, J., Ridgway, S. T., Jameson, R., Haas, M., & Lenzen, R. 1993, A&A, 278, 129
Lin, D. N. C., Hayashi, M., Bell, K. R., & Ohashi, N. 1994, ApJ, 435, 821
Masson, C. R., & Chernin, L. M. 1993, ApJ, 414, 230
Mathieu, R. D., Adams, F. C., & Latham, D. W. 1991, AJ, 101, 2184
Mouschovias, T. Ch. 1976, ApJ, 207, 141
———. 1991, in The Physics of Star Formation and Early Stellar Evolution, ed. C. J. Lada & N. D. Kylafis (Dordrecht: Kluwer), 100
Mundt, R., Ray, T. P., & Bührke, T. 1988, ApJ, 333, L69
Myers, P. C., Fuller, G. A., Goodman, A. A., & Benson, P. J. 1991, ApJ, 376, 561
Nakamura, F., Hanawa, T., & Nakano, T. 1995, ApJ, 444, 770
Ohashi, N., & Hayashi, M. 1995, Ap&SS, 224, 13
Osterloh, M., & Beckwith, V. W. 1995, ApJ, 439, 288
Sargent, A. I., & Beckwith, S. 1991, ApJ, 382, L31
Shu, F. H. 1977, ApJ, 214, 488
Spitzer, L. 1978, Physical Processes in the Interstellar Medium (New York: Wiley), 283
Stapelfeldt, K. R., et al. 1995, ApJ, 449, 888
Staude, H. J., & Elsässer, H. 1993, Astron. Astrophys. Rev., 5, 165
Terebey, S., Shu, F. H., & Cassen, P. 1984, ApJ, 286, 529 (TSC)
Ulrich, R. K. 1976, ApJ, 210, 377
Weintraub, D. A., Kastner, J. H., & Whitney, B. A. 1995, preprint
Whitney, B. A., & Hartmann, L. 1992, ApJ, 395, 529
———. 1993, ApJ, 402, 605
Wolfire, M. G., & Cassinelli, J. P. 1987, ApJ, 319, 850
Yorke, H. W., Bodenheimer, P., & Laughlin, G. 1993, ApJ, 411, 274
Zinnecker, H., McCaughrean, M. J., & Wilking, B. A. 1993, in Protostars and Planets III, ed. E. H. Levy & J. Lunine (Tucson: Univ. Arizona Press), 429

© American Astronomical Society • Provided by the NASA Astrophysics Data System